

A highly ionized stellar bow shock in the Small Magellanic Cloud

William J. Henney¹*, S. J. Arthur¹, M. Valerdi², Jesús A. Toalá¹, Peter Zeidler³

¹Instituto de Radioastronomía y Astrofísica, Universidad Nacional Autónoma de México, Apartado Postal 3-72, 58090 Morelia, Michoacán, Mexico

²Instituto Nacional de Astrofísica, Óptica y Electrónica, Luis Enrique Erro #1, Tonantzintla, 72840 Puebla, México

³AURA for the European Space Agency (ESA), ESA Office, Space Telescope Science Institute, 3700 San Martin Drive, Baltimore, MD 21218, USA

Submitted: October 18, 2025

ABSTRACT

We report the discovery of a parsec-scale stellar bow shock associated with the O2 III(f) star Walborn 3 in the cluster NGC 346 of the Small Magellanic Cloud. The bow shock is most clearly detected in optical He II and [Ar IV] emission lines but is also seen at mid-infrared wavelengths between 12 μm and 24 μm. There is no evidence that the star is a runaway, rather the bow shock is likely due to interaction of the stellar wind with streaming motions of the photoionized gas within the N66 H II region.

Key words: Atomic physics – Circumstellar matter – Stars: winds, outflow

1 INTRODUCTION

The interaction of a star's wind with the surrounding medium can result in an arc-shaped circumstellar emission nebula, frequently referred to as a bow shock (Gull & Sofia 1979; van Buren & McCray 1988). Stellar bow shocks are found around a wide variety of different stars, including pre-main sequence stars (Bally & Reipurth 2001; Henney et al. 2013), neutron stars (Cordes et al. 1993), and cool giants and supergiants (Sahai & Chronopoulos 2010; Cox et al. 2012), but they are most commonly associated with hot luminous OB stars (van Buren et al. 1995; Kobulnicky et al. 2016). Bow shocks are most frequently observed via their infrared continuum emission (Meyer et al. 2016), which arises from dust grains that are heated by the stellar radiation field (Draine & Li 2007), but specific classes of bow shock have also been identified via multiple thermal and non-thermal emission mechanisms that trace gas and plasma components. The emission arcs are most commonly interpreted as due to the hydrodynamic interaction induced by supersonic relative motion of the star with respect to the ambient material (Wilkin 1996), but models involving a subsonic interaction have also been proposed (Mackey et al. 2015, 2016). Also, the role of the stellar wind ram pressure in supporting the arc may be replaced by radiation pressure in some cases, see Henney & Arthur (2019a,b,c).

Stellar bow shocks can be used to estimate stellar wind mass loss rates by applying momentum-balance arguments (Gvaramadze et al. 2012; Kobulnicky et al. 2018, 2019; Henney & Arthur 2019c). These provide an important check on more traditional spectroscopic methods (Hillier 2020), since the systematic uncertainties and biases are different. Line-driven wind theory for hot stars predicts that momentum-loss rates should increase with metallicity, Z , as $\dot{M}V_w \propto Z^n$ with $n = 0.6\text{--}0.8$ (Vink et al. 2001; Krtička & Kubát 2018; Vink & Sander 2021; Björklund et al. 2021) for the most luminous stars ($L > 10^6 L_\odot$).

The closest low-metallicity stellar populations ($Z = 0.1$ to $0.2Z_\odot$,

Narloch et al. 2021) are found in the Small Magellanic Cloud (SMC) at a distance of 62 kpc (Graczyk et al. 2020). A small number of stellar bow shocks have been previously identified in the SMC (Gvaramadze et al. 2011; Sheets et al. 2013) by means of their mid-infrared dust emission. The majority of these sources are found far from the cores of dense clusters and are probably *runaways* (Blaauw 1961), which have been ejected from a binary system or stellar cluster (Hoogerwerf et al. 2001; Renzo et al. 2019). In the Milky Way, a second class of stellar bow shocks are found inside young massive star clusters: *weather vanes* (Povich et al. 2008), which have low space velocities and are interacting with streaming motions of the local interstellar medium, such as champagne flows (Tenorio-Tagle 1979).

In this paper, we report the discovery of just such a bow shock inside the massive stellar cluster NGC 346, which excites the H II region N66 (Henize 1956). The bow shock is associated with the very early-type star Walborn 3 (W 3) (Walborn & Blades 1986), also known as MPG 355 (Massey et al. 1989) with spectral type ON2 III(f*) (Heydari-Malayeri & Selier 2010).

Atmosphere models of Rivero González et al. (2012)

2 MUSE SPECTRAL MAPPING

The primary observational data set used in this paper is an archival integral field spectral cube of NGC 346 obtained with the MUSE spectrograph (Bacon et al. 2010, 2014) on the VLT as part of program 098.D-0211(A) (PI: W.-R. Hamann). The usable field of view is approximately 64 arcsec times 60 arcsec with spaxel size of 0.2 arcsec and estimated seeing full-width half maximum (FWHM) width of 0.961 arcsec. The spectral range is 4595 Å to 9366 Å sampled at 1.25 Å pix⁻¹ and the spectral resolving power varies from $R \approx 2000$ in the blue to $R \approx 4000$ in the red. We use reduced data from the standard ESO pipeline processing (Weilbacher et al. 2020), co-added across multiple observations obtained on 2016-08-22 with a total effective exposure time of 12 600 s.

We divide the spectral range into sections of width 800 Å and fit a 6th order polynomial to the continuum in line-free wavelengths of

* w.henney@irya.unam.mx

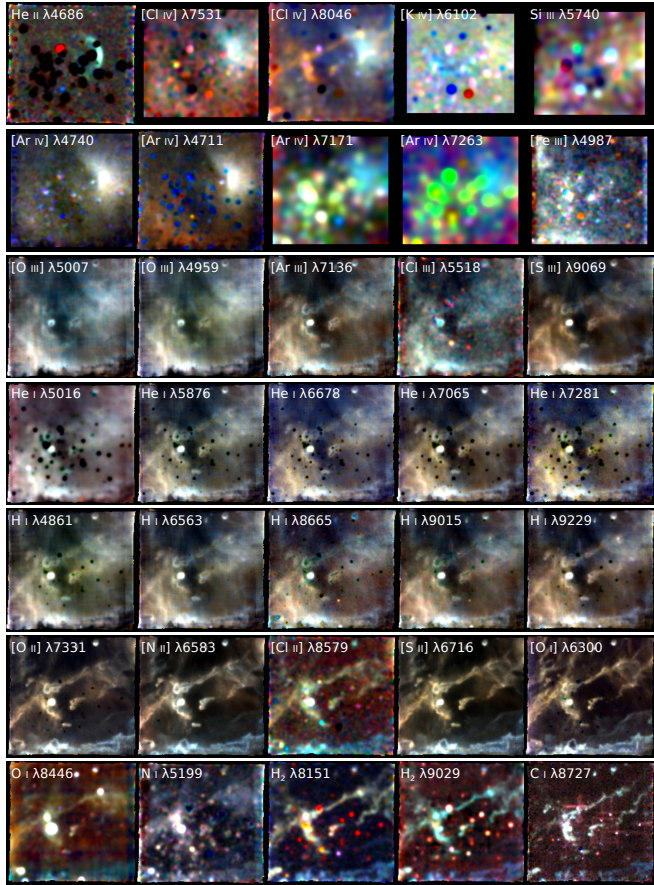


Figure 1. Emission line maps of the core of NGC 346 derived from the MUSE data cube.

each section, using an independent fit for each spaxel. We then extract individual emission lines (or close blends) from the continuum-subtracted spectra using 5 Å windows, centered on the expected wavelength of each line in the systemic frame of the nebula (heliocentric velocity $V \approx +160$ km s $^{-1}$). We correct for an over-subtraction of the sky background, which is apparent in the pipeline-processed data cube. We establish accurate zero points for all lines by checking that multiple line ratios tend towards physically reasonable asymptotes as the brightness tends towards zero.

We use the observed Balmer decrement between H α and H β to correct all lines for foreground dust extinction, assuming an SMC-appropriate reddening law with $R_V = 2.74$ (Fitzpatrick & Massa 1990; Bouret et al. 2003). The reddening is low over most of the field ($E(B-V) \approx 0.1$) but reaches $E(B-V) \approx 1$ along the southern edge (labeled “foreground filament” in Figure 2b).

2.1 Detection of a high-ionization bow shock

An east-facing bow shock structure is detected around the star Walborn 3, as mapped in Figure 2, with emission line brightness profiles shown in Figure 3. The correspondence between different emission lines and the ionization state of the gas is illustrated in Figure 4, which explains the definitions of low, medium, and high ionization that we employ in this paper.

Figure 2a shows that the inner edge of the bow shock is traced by a

sharp ridge of the highest ionization He II λ4686 emission (red), while [Ar IV] λ4740 emission (green) is more extended and has a diffuse outer boundary. Nebular emission from the same field in medium and low ionization lines is shown in Figure 2b, from which one sees that there is no clear evidence for the bow shock in these lines. Instead, the low ionization lines ([O I], red, and [S II], green) trace the ionization fronts at the surface of dense filaments and globules, while the medium ionization line ([S III], blue) traces diffuse ionized gas in the interior of the nebula that is largely unrelated to the bow shock.

Figure 2c shows the position of the MUSE field (orange box) on a wider scale *HST* image of the N66 H II region (Nota et al. 2006). The head of the bow shock is oriented towards the bright N–S oriented filament that is located outside of the MUSE field to the West, and which represents a large scale ionization front at the edge of the H II region. The supernova remnant SNR J59.4–7210 is centered roughly 1 arcmin to the East of the H II region, but based on the X ray emission (Maggi et al. 2019) it does not overlap the MUSE field.

Figure 2d shows a zoomed view of the *HST* H α image around W 3, compared with contours of the bow shock emission. The H α brightness does appear to be slightly higher within the bow shock contours than just outside it, but the effect is subtle compared with the general fluctuations in H α brightness in the nebula.

2.2 Brightness profiles along the bow shock axis

Figure 3a shows surface brightness profiles in multiple emission lines along an East–West cut along the bow shock axis. The He II emission peak lies at an offset 4 arcsec west from the star W 3, with a width (FWHM) of about 2 arcsec (note that 1 arcsec ≈ 0.3 pc at the distance of the SMC). If the He II line is due to recombination of He $^{+2}$, then a hard radiation field with $h\nu > 54.4$ eV is required in order to photoionize He $^+$ (see Figure 4). The He II brightness becomes negative close to the star position due to contamination by the photospheric absorption line. The [Ar IV] emission peak lies slightly farther from the star (4.5 arcsec) and shows a gradual linear decline with FWHM ≈ 20 arcsec. In both lines, diffuse nebular emission is undetectably small in the regions adjoining the bow shock. The medium ionization lines, on the other hand, are dominated by the large-scale nebular emission and vary by a factor of only 1.5 to 2 along the entire slit. Nonetheless, there is an apparent rise in the brightness of these lines at the position of the bow shock (see gray box in Figure 3) that tracks the rise and fall of the [Ar IV] line. This increase amounts to about 50% of the diffuse nebula emission in the case of [O III] and the H and He recombination lines but only about 30% in the case of [Ar III], which arises from lower ionization conditions than [O III], as shown in Figure 4.

Figure 3b shows even lower ionization emission, as traced by [S III] and [S II] lines, together with electron temperature and density profiles derived from the emission line ratios [S III] λ6312/λ9069 and [S II] λ6716/λ6731. The rise at the bow shock position is very weak in [S III] (about 15% of the diffuse nebula brightness) and it is completely absent in [S II]. The peaks in the [S II] profile at offsets of 7 arcsec and 12 arcsec correspond to ionization fronts of background globules, as seen in Figure 2b. The 12 arcsec peak is also visible in [S III] and the other medium ionization lines of panel a, but with lower contrast.

A broad maximum in [S III] lies at an offset of –3 arcsec and is labeled “medium-ionization peak” in the figure. It corresponds to wispy H α emission seen in the HST image of Figure 2d immediately to the left of W 3. The same peak is also visible in the other medium ionization lines of Figure 3a, but the contrast decreases markedly as

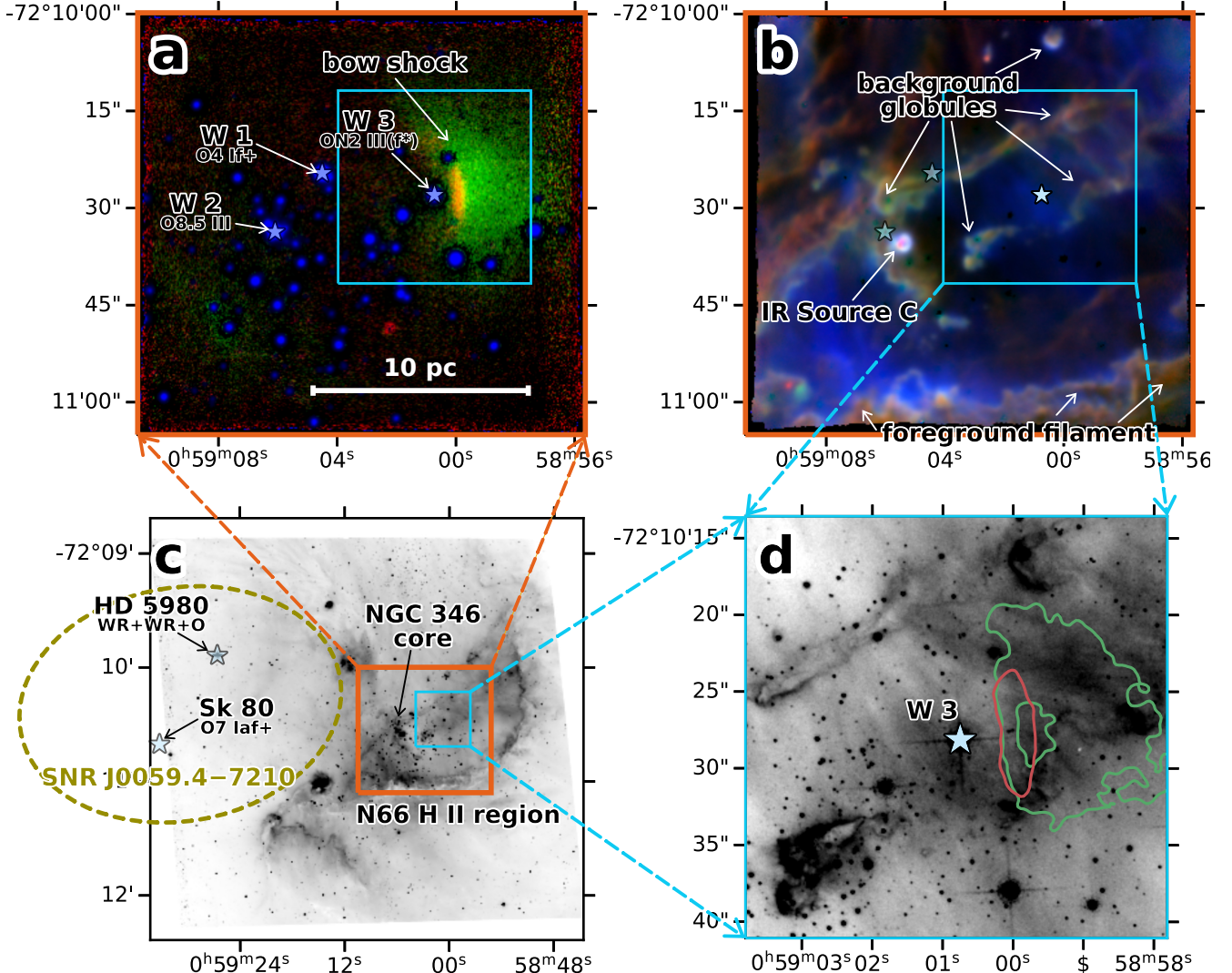


Figure 2. MUSE emission line images of the core of NGC 346. (a) High-ionization emission from the bow shock. Red shows $\text{He II } \lambda 4686$, green shows $[\text{Ar IV}] \lambda 4740$, blue shows continuum emission at 4700 \AA (mainly starlight). Star symbols indicate the positions of the most luminous ionizing stars in the cluster: Walborn 1, 2, and 3. (b) Medium to low-ionization emission from the surrounding N66 H II region. Red shows $[\text{O I}] \lambda 6300$, green shows $[\text{S II}] \lambda 6731$, blue shows $[\text{S III}] \lambda 9069$. (c) Location of the MUSE field within the wider nebula against a background $\text{H}\alpha$ image from HST-ACS in the F658N filter. The yellow dashed ellipse shows the maximum extent of the X-ray emission from the supernova remnant SNR J59.4–7210, while star symbols indicate more distant luminous ionizing stars. (d) Zoom of panel c showing detail of the bow shock region in the light of $\text{H}\alpha$ emission, with superimposed contours of He II (red) and $[\text{Ar IV}]$ (green).

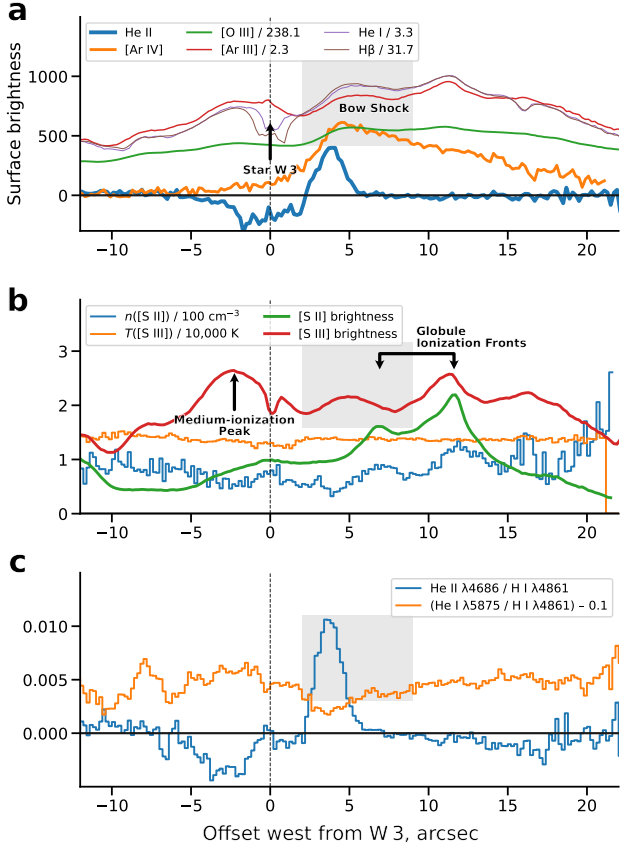


Figure 3. (a) Continuum-subtracted and extinction-corrected line surface brightness profiles along an East–West cut along the bow shock axis of width 4 arcsec, derived from MUSE integral field spectra. The gray box indicates the leading edge of the bow shock emission for comparison with following figures. Thickest lines show the high ionization emission from He II $\lambda 4686$ (blue) and [Ar IV] $\lambda 4740$ (orange). Progressively thinner lines show medium ionization emission from [O III] $\lambda 5007$ (green), [Ar III] $\lambda 7136$ (red), He I $\lambda 5875$ (purple), and H β $\lambda 4861$ (brown). Vertical scale gives brightness in instrument units, for conversion to cgs multiply by 1.489×10^{-8} erg s $^{-1}$ cm $^{-2}$ sr $^{-1}$. The brightness of medium ionization lines have been scaled by factors given in the key, so as to make all the lines approximately coincide at the left edge of the gray box. (b) As panel a but showing the [S II] density (orange) and [S III] temperature (blue), together with the brightness profiles of [S II] $\lambda 6731$ (red) and [S II] $\lambda 9069$ (green) on an arbitrary scale. (c) As panel a but showing line ratios of He II/H I (blue) and He I/H I (orange). A constant value of 0.1 has been subtracted from the latter for ease of comparison and to emphasise the slight dip in He I/H I at the position of the bow shock.

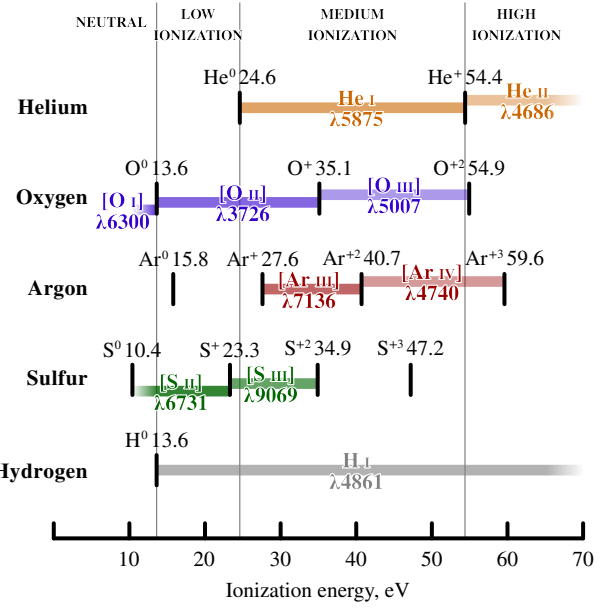


Figure 4. Classification of optical emission lines by degree of ionization. The broad ionization zones are defined by the H and He opacity: neutral ($H^0 + He^0$), low ionization ($H^+ + He^0$), medium ionization ($H^+ + He^+$), and high ionization ($H^+ + He^{+2}$). Within each zone, the ionization of metals will vary according to the local ionizing flux spectrum and electron density, depending on the ionization energy of each ion. The latter is indicated in the figure for selected elements, together with the range of ionization where different lines will be emitted, assuming that forbidden lines are excited solely by electron collisions, while permitted lines are excited solely by recombinations.

one passes from [S III], through [Ar III], to [O III], which is a sequence of increasing ionization (see Figure 4).

The disparate ionization-dependent behaviors of the three regions are summarised in Figure 7, which shows the excess emission relative to the diffuse nebula for the bow shock, the medium-ionization peak, and the globule ionization fronts. Note that He II and [Ar IV] are not included in this figure since they have effectively infinite contrast.

3 FORS1 LONGSLIT OBSERVATIONS

To complement the MUSE data, we employ longslit optical spectra first presented by ?, which were obtained with the Focal Reducer Low Dispersion Spectrograph (FORS1) on the VLT. One of the EW-oriented slit positions serendipitously crosses the W3 bow shock. Although the spectral resolution of these data is slightly lower than that of MUSE, the wavelength coverage extends further towards the blue, allowing study of additional lines such as [O III] $\lambda 4363$ and [Ne III] $\lambda 3869$. In addition, the slit length of 410 arcsec is much longer than the MUSE field of view of 60 arcsec.

Results from the FORS1 data are shown in Figure 5. The upper panel shows the temperature-sensitive line ratio [O III] $\lambda 4363 / \lambda 5007$, which is discussed further in section 5 below. The lower panel shows the surface brightness profiles of selected emission lines from a variety of ionization stages as a function of position measured in arc seconds from the star W 3 (positive values to the West). The bow shock rim region (indicated by the light gray box) is very small on the scale of this plot but is clearly detected in the He II, [Ar IV],

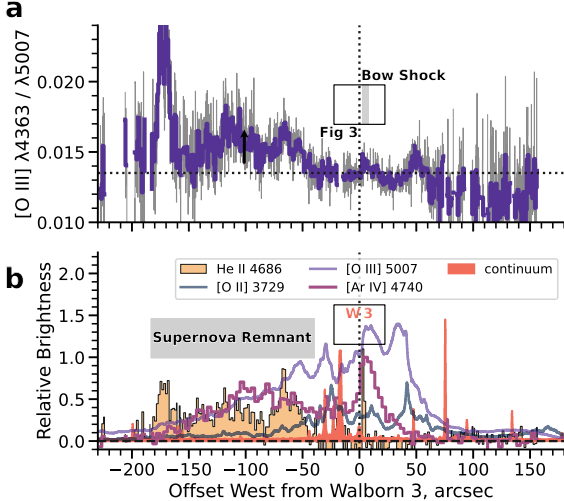


Figure 5. Emission line surface brightness profiles and line ratios along a large-scale East–West cut across the entire region, based on FORS1 longslit spectra. The slit is close to the symmetry axis of the bow shock. (a) Temperature-sensitive line ratio $[\text{O III}] 4363/\lambda 5007$. The gray box shows the same inner rim region of the bow shock that is highlighted by a gray box in Fig. 3. (b) Selected emission lines from a wide range of ionization stages.

and $[\text{O III}]$ profiles. However, although the bow shock is the brightest source of He II emission within the MUSE field, it is not particularly prominent on the larger scales revealed by FORS1. Instead, the He II emission (light orange shaded histogram in figure) is dominated by extensive bright emission in the East of the region, at offsets from -180 to -50 arcsec, which coincides with the location of the supernova remnant SNR B0057–72.2 (Ye et al. 1991).

4 MID-INFRARED EMISSION

To supplement the optical data, we use mid-infrared spectral imaging from Spitzer/IRS (Houck et al. 2004). *Jesús: add a few more details here.* The spectra were decomposed into atomic emission lines, polycyclic aromatic hydrocarbon (PAH) emission features, and continuum bands. These are illustrated as three-color RGB images in Figure 6. Panels a and b show that the bow shock is particularly prominent in the continuum bands between 13 and $18 \mu\text{m}$ (red channel in panel a, blue channel in panel b). Panel c shows a close-up of the region of the MUSE field of view, with contours of the optical $[\text{Ar IV}]$ emission overlaid in white onto the infrared image. Here it can be seen that although there is a broad agreement between the morphology of the $[\text{Ar IV}]$ and the 13 – $14 \mu\text{m}$ continuum, the latter is brighter towards the south side of the bow shock.

Panels d and e of Figure 6 show infrared emission lines that trace the ionization structure of the region. Panel d shows gradations of ionization in the H II region from high ionization ($[\text{S IV}] 10.5 \mu\text{m}$, red) through medium ionization ($[\text{Ne III}] 15.5 \mu\text{m}$, green) to low ionization ($[\text{Ne II}] 12.8 \mu\text{m}$, blue). The bow shock shows as a bright orange feature in this image, indicating predominantly $[\text{S IV}]$ emission with some contribution from $[\text{Ne III}]$. Panel e shows the transition from the H II region to the PDR from medium ionization ($[\text{S III}] 18.7 \mu\text{m}$, red, and $33.4 \mu\text{m}$, green) to partially ionized and neutral ($[\text{Si II}] 34.8 \mu\text{m}$, blue). The bow shock is not prominent in any of these lines.

Lots of this was anticipated by Contursi et al. (2000) With ISO observations, see their Fig. 13. Quote: “We remark that this region is

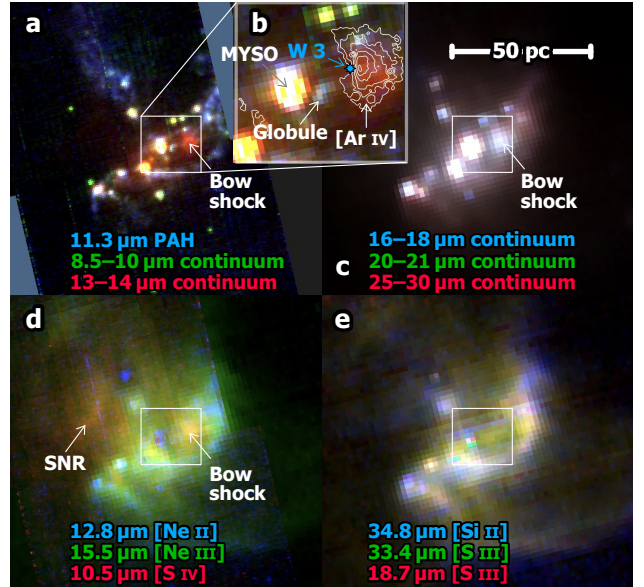


Figure 6. Spectral imaging of the NGC 346/N66 region with *Spitzer* IRS. Each panel is an RGB combination of three spectral ranges or features. (a) Shorter wavelength mid-infrared dust emission: $11.3 \mu\text{m}$ PAH feature (blue), $8 \mu\text{m}$ to $9 \mu\text{m}$ continuum (green), $13 \mu\text{m}$ to $14 \mu\text{m}$ continuum (red). The emission from the bow shock is most prominent in the red channel and is indicated by a white arrow. (b) Zoom of panel a showing central core of NGC 346 with the star Walborn 3 indicated in blue and with superimposed white contours of optical $[\text{Ar IV}]$ emission. (c) Longer wavelength mid-infrared dust emission: $16 \mu\text{m}$ to $18 \mu\text{m}$ continuum (blue), $20 \mu\text{m}$ to $21 \mu\text{m}$ continuum (green), $25 \mu\text{m}$ to $30 \mu\text{m}$ continuum (red). In this image the bow shock is most prominent in the blue channel. (d) Shorter wavelength mid-infrared emission lines: $[\text{Ne II}] 12.8 \mu\text{m}$ (blue), $[\text{Ne III}] 15.5 \mu\text{m}$ (green), $[\text{S IV}] 10.5 \mu\text{m}$ (red). In this image the bow shock is most prominent in the red channel. (e) Longer wavelength mid-infrared emission lines: $[\text{Si II}] 34.8 \mu\text{m}$ (blue), $[\text{S III}] 33.4 \mu\text{m}$ (green), $[\text{S III}] 18.7 \mu\text{m}$ (red). In this image the bow shock is not prominent in any channel.

close to the earliest-type star of N66 ($O\text{III}(f^*)$) suggesting that here the ISRF is not only very strong but also very hard. This results in a complete destruction of the AIB carriers and partially also of the smallest VSGs.”

Also previous Spitzer work by Whelan et al. (2013), but I do not like their Figure 11 where they plot the correlation between the ratio of $14 \mu\text{m}$ continuum over $[\text{S IV}]$ to $[\text{S IV}]$ over $[\text{Ne II}]$. With no correlation between the three, we would get the observed correlation in the ratios.

5 ELECTRON DENSITY AND TEMPERATURE

The electron density of low ionization gas (orange histogram in Figure 3b) is calculated from the $[\text{S II}]$ nebular lines using PyNeb (Luridiana et al. 2015) with radiative rates from Rynkun et al. (2019) and collisional rates from Tayal & Zatsarinsky (2010). Typical values are around 70 cm^{-3} , rising to 150 cm^{-3} at the globule ionization fronts. Brighter globules elsewhere in the field show densities higher than 1000 cm^{-3} . We also attempted to measure the density in medium ionization gas using the $[\text{Cl III}]$

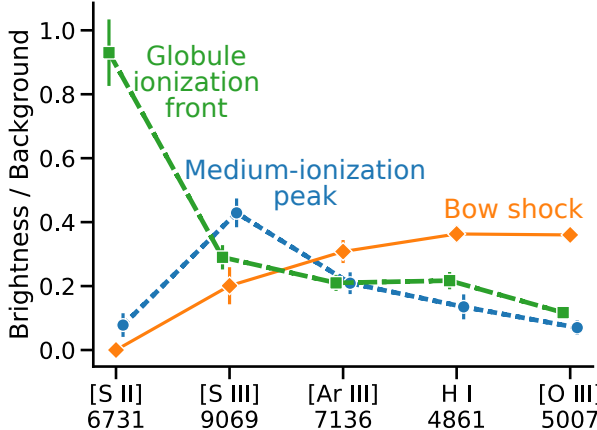


Figure 7. Maximum brightness contrast in low to medium ionization lines for the bow shock (orange), globule ionization front (green dashed), and medium-ionization peak (blue dotted). All values are relative to the diffuse background nebula emission. Emission lines are arranged in order of increasing ionization from left to right.

5.1 [Ar IV] diagnostics

We analyze the auroral and nebula lines of [Ar IV] following the approach of Keenan et al. (1997).

Apart from the inner rim of the bow shock, there is no diffuse He II emission in the core of NGC 346, or in the western side of the N66 region. The eastern side of N66, on the other hand, shows extensive He II $\lambda 4686$ emission, as can be seen at offsets from -200 to -50 arcsec in Figure 5b. The eastern side of N66 also shows a ten times higher $[\text{Fe III}] / \text{H}\beta$ ratio and disturbed kinematics in low-ionization lines such as [S II]. All these are probably due to a foreground supernova remnant SNR B0057–72.2 (Ye et al. 1991) that overlaps with this part of the nebula (Chu & Kennicutt 1988; Nazé et al. 2002; Danforth et al. 2003; Maggi et al. 2019; Matsuura et al. 2022).

6 DISCUSSION

Is there any possibility it might be a runaway?

What is the reason that we detect this bow shock at optical wavelengths, which is not typical? Probably due to the presence of the high ionization stages, which allow the weak bow shock emission to be separated from the background hii region. This is similar to the argument of (Danforth et al. 2003) as to why it is better to use UV observations to find SNR in bright hii regions.

7 CONCLUSIONS

ACKNOWLEDGEMENTS

We gratefully acknowledge financial support provided by Dirección General de Asuntos del Personal Académico, Universidad Nacional Autónoma de México, through grants “Programa de Apoyo a Proyectos de Investigación e Innovación Tecnológica IN109823 and XXXXXXXX”.

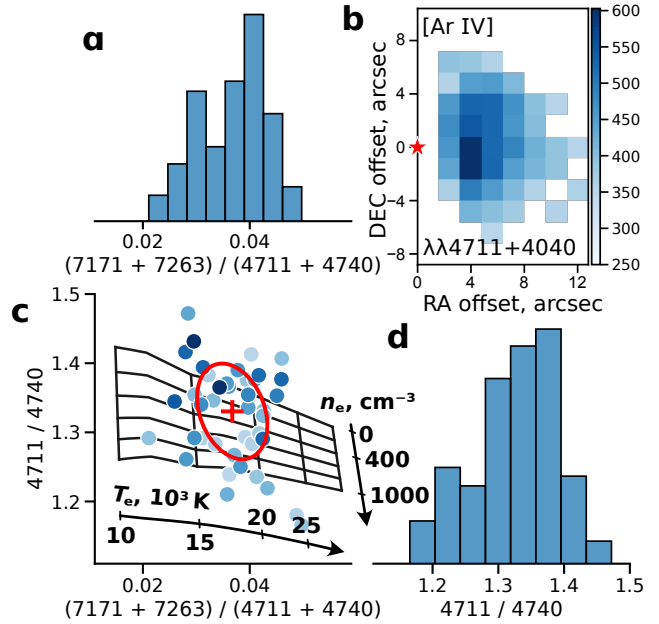


Figure 8. Temperature and density diagnostics of the bow shock from [Ar IV] line ratios.

References

- Bacon R., et al., 2010, in Proc. SPIE p. 773508, doi:10.1117/12.856027
- Bacon R., et al., 2014, The Messenger, 157, 13
- Bally J., Reipurth B., 2001, ApJ, 546, 299
- Björklund R., Sundqvist J. O., Puls J., Najarro F., 2021, A&A, 648, A36
- Blaauw A., 1961, Bull. Astron. Inst. Netherlands, 15, 265
- Bouret J. C., Lanz T., Hillier D. J., Heap S. R., Hubeny I., Lennon D. J., Smith L. J., Evans C. J., 2003, ApJ, 594, 279
- Chu Y.-H., Kennicutt Robert C. J., 1988, AJ, 95, 1111
- Contursi A., et al., 2000, A&A, 362, 310
- Cordes J. M., Romani R. W., Lundgren S. C., 1993, Nature, 362, 133
- Cox N. L. J., et al., 2012, A&A, 537, A35
- Danforth C. W., Sankrit R., Blair W. P., Howk J. C., Chu Y.-H., 2003, ApJ, 586, 1179
- Draine B. T., Li A., 2007, ApJ, 657, 810
- Fitzpatrick E. L., Massa D., 1990, ApJS, 72, 163
- Graczyk D., et al., 2020, ApJ, 904, 13
- Gull T. R., Sofia S., 1979, ApJ, 230, 782
- Gvaramadze V. V., Pfleider-Altenburg J., Kroupa P., 2011, A&A, 525, A17
- Gvaramadze V. V., Langer N., Mackey J., 2012, MNRAS, 427, L50
- Henize K. G., 1956, ApJS, 2, 315
- Henney W. J., Arthur S. J., 2019a, MNRAS, 486, 3423
- Henney W. J., Arthur S. J., 2019b, MNRAS, 486, 4423
- Henney W. J., Arthur S. J., 2019c, MNRAS, 489, 2142
- Henney W. J., García-Díaz M. T., O'Dell C. R., Rubin R. H., 2013, MNRAS, 428, 691
- Heydari-Malayeri M., Selier R., 2010, A&A, 517, A39
- Hillier D. J., 2020, Galaxies, 8, 60
- Hoogerwerf R., de Bruijne J. H. J., de Zeeuw P. T., 2001, A&A, 365, 49
- Houck J. R., et al., 2004, ApJS, 154, 18
- Keenan F. P., McKenna F. C., Bell K. L., Ramsbottom C. A., Wickstead A. W., Aller L. H., Hyung S., 1997, ApJ, 487, 457
- Kobulnicky H. A., et al., 2016, ApJS, 227, 18
- Kobulnicky H. A., Chick W. T., Povich M. S., 2018, ApJ, 856, 74 (K18)
- Kobulnicky H. A., Chick W. T., Povich M. S., 2019, AJ, 158, 73
- Krtička J., Kubát J., 2018, A&A, 612, A20
- Luridiana V., Morisset C., Shaw R. A., 2015, A&A, 573, A42

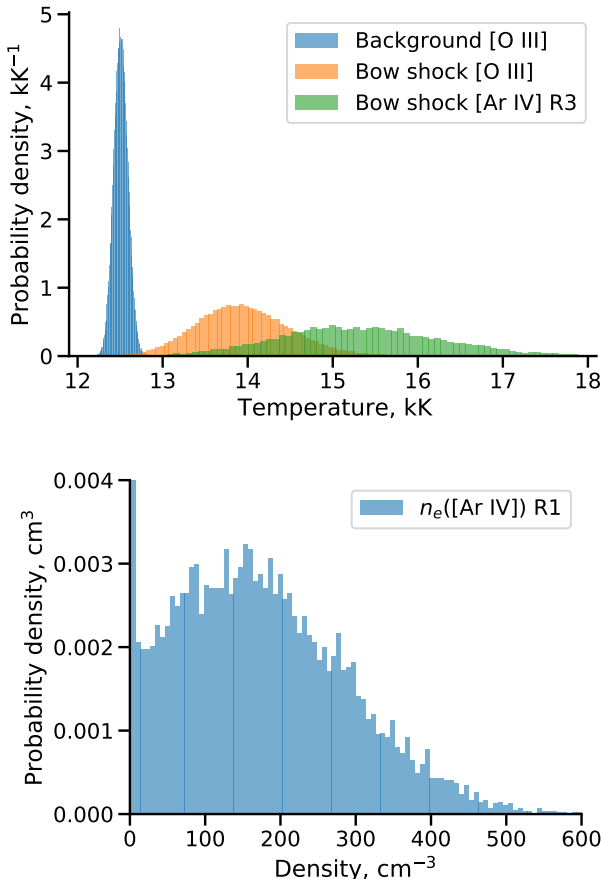


Figure 9. Derived temperature of nebula and bow shock from FORS longslit observations.

- Mackey J., Gvaramadze V. V., Mohamed S., Langer N., 2015, A&A, 573, A10
 Mackey J., Haworth T. J., Gvaramadze V. V., Mohamed S., Langer N., Harries T. J., 2016, A&A, 586, A114
 Maggi P., et al., 2019, A&A, 631, A127
 Massey P., Parker J. W., Garmany C. D., 1989, AJ, 98, 1305
 Matsuura M., et al., 2022, MNRAS, 513, 1154
 Meyer D. M.-A., van Marle A.-J., Kuiper R., Kley W., 2016, MNRAS, 459, 1146
 Narloch W., et al., 2021, A&A, 647, A135
 Nazé Y., Hartwell J. M., Stevens I. R., Corcoran M. F., Chu Y. H., Koenigsberger G., Moffat A. F. J., Niemela V. S., 2002, ApJ, 580, 225
 Nota A., et al., 2006, ApJ, 640, L29
 Povich M. S., Benjamin R. A., Whitney B. A., Babler B. L., Indebetouw R., Meade M. R., Churchwell E., 2008, ApJ, 689, 242
 Renzo M., et al., 2019, A&A, 624, A66
 Rivero González J. G., Puls J., Massey P., Najarro F., 2012, A&A, 543, A95
 Rynkun P., Gaigalas G., Jönsson P., 2019, A&A, 623, A155
 Sahai R., Chronopoulos C. K., 2010, ApJ, 711, L53
 Sheets H. A., Bolatto A. D., van Loon J. T., Sandstrom K., Simon J. D., Oliveira J. M., Barbá R. H., 2013, ApJ, 771, 111
 Tayal S. S., Zatsariny O., 2010, ApJS, 188, 32
 Tenorio-Tagle G., 1979, A&A, 71, 59
 Vink J. S., Sander A. A. C., 2021, MNRAS, 504, 2051
 Vink J. S., de Koter A., Lamers H. J. G. L. M., 2001, A&A, 369, 574
 Walborn N. R., Blades J. C., 1986, ApJ, 304, L17
 Weilbacher P. M., et al., 2020, A&A, 641, A28

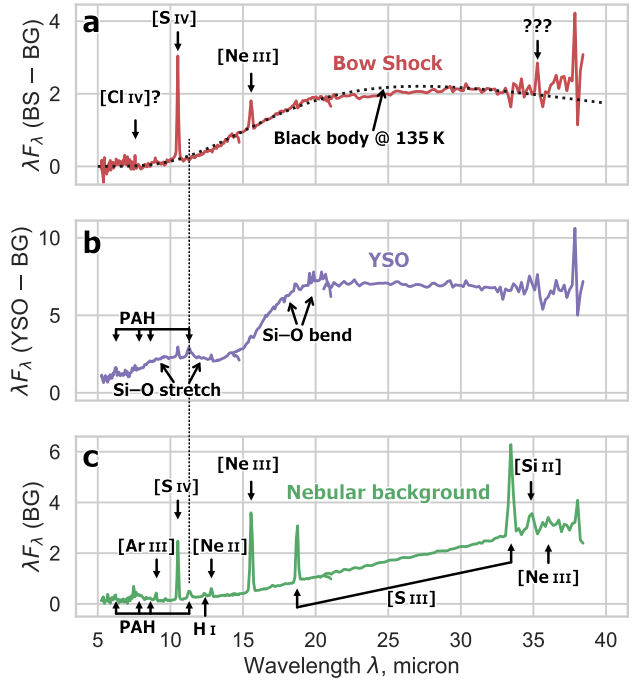


Figure 10. Mid-infrared Spitzer spectra of (a) background-subtracted bow shock, (b) background-subtracted mYSO C, (c) nebula background emission.

Whelan D. G., Lebouteiller V., Galliano F., Peeters E., Bernard-Salas J., Johnson K. E., Indebetouw R., Brandl B. R., 2013, ApJ, 771, 16
 Wilkin F. P., 1996, ApJ, 459, L31
 Ye T., Turtle A. J., Kennicutt R. C. J., 1991, MNRAS, 249, 722
 van Buren D., McCray R., 1988, ApJ, 329, L93
 van Buren D., Noriega-Crespo A., Dgani R., 1995, AJ, 110, 2914

This paper has been typeset from a TeX/LaTeX file prepared by the author.

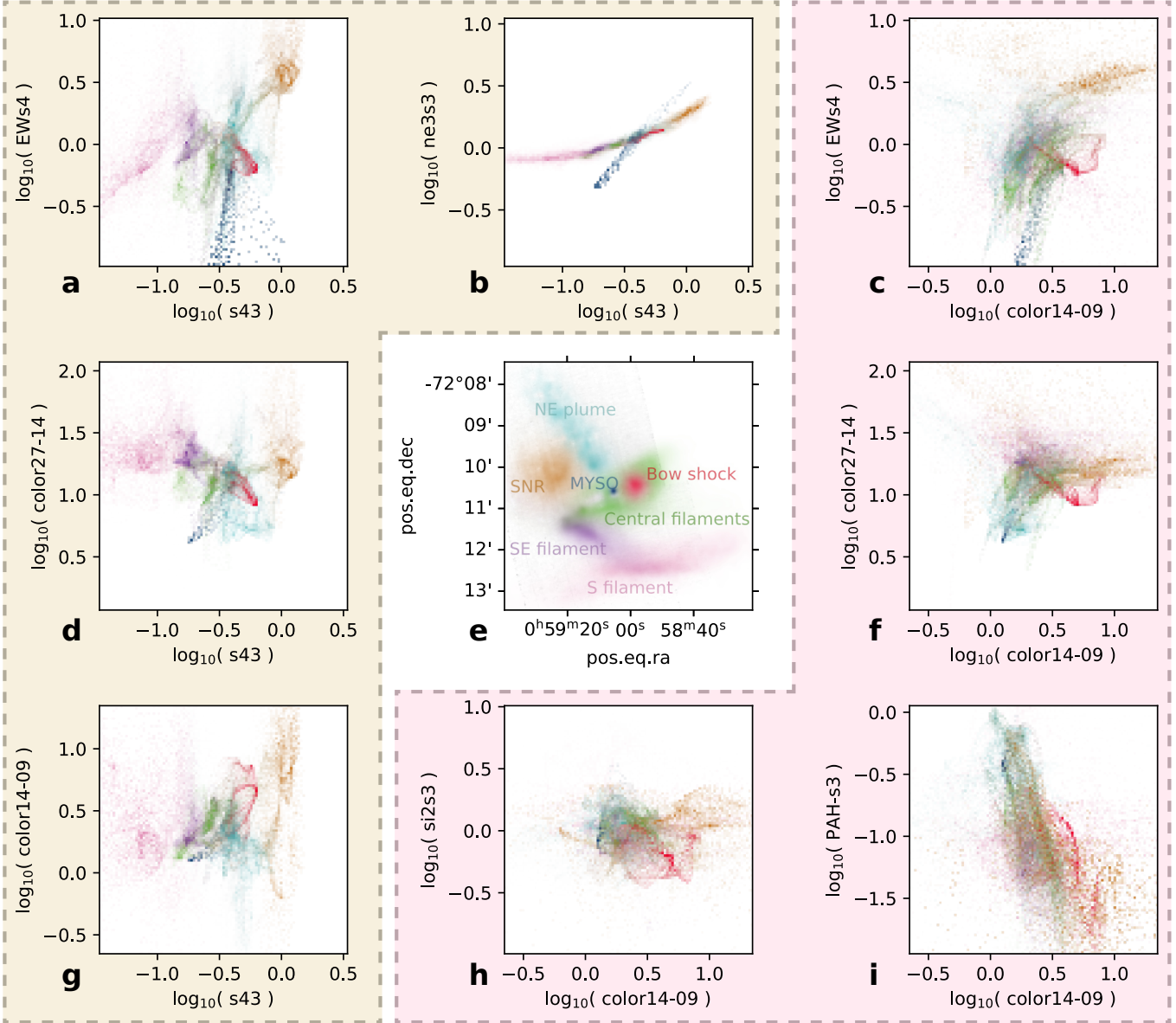


Figure 11. Mid-infrared ratio-ratio correlations for different spatial zones in NGC 346.